with IR transmissivity like that of the metallic phase (i.e., collapse of the optical band gap to below 0.25 eV) even without melting the CDW order. In this state the PLD of the insulating phase remains intact, but the valence charge distribution is altered. The nature of the changes in charge density can be understood from the symmetry of the changes in diffraction (Fig. 2F), the orbitals (Fig. 4B), and the difference PDF (Fig. 3B). The negative features at 1.3 Å and 4.4 Å in Fig. 3B suggest an increase in the filling of the d_{xy} subshell that contributes most strongly to the CDW along $\mathbf{c}_R$. The positive features at 0.8 Å and 1.9 Å suggest reduced filling of the d_{xz} subshell, which reduces charge density on the V and O atoms in the octahedral chains. The d_{yz} states oriented orthogonal to $\mathbf{c}_R$, which are understood to be unoccupied in semiconducting VO_2 (*15*, *22*), remain unchanged. Thus, optical excitation with fluences below the threshold required to melt the PLD drives a 1D redistribution of occupancy in the d_{xy} and d_{xz} subshells, not a transformation to the isotropic state of the equilibrium metal. Suppression of correlation-induced splitting into upper (UHB) and lower (LHB) Hubbard bands, either preferentially in the d_{xz} band (Fig. 4A, iv) or in both d_{xz} and d_{xy} shells (Fig. 4A, ii), could lead to such a reorganization. The first case represents an optically induced orbital-selective transition with a mixture of localized (d_{xy}) and itinerant (d_{xz}) behavior (*34*).

The picosecond time scale of this transformation, in addition to its long-lived nature, suggests that the increased vibrational excitation of the lattice due to carrier relaxation (electron-phonon coupling) is a key factor in both inducing and maintaining the reorganization. The nonequilibrium population of excited carriers relaxes within 1 ps in thin VO_2 films grown by pulsed laser deposition (*27*). However, our measurements cannot rule out the possibility of other mechanisms affecting this stability, including kinetic trapping of the valence charge reorganization. Earlier work identified metal-like phases of VO_2 with properties distinct from that of the rutile, high-temperature metal. This includes nanoscale correlated metallic domains with unidentified lattice structure that were observed near the transition temperature (*35*, *36*), as well as the observation that the thermally initiated semiconductor-to-metal transition and the SPT can occur noncongruently, suggesting the presence of a metal-like *M*1 phase of VO_2 (*37*). The correlated metallic state observed in the thermally activated phase transition and the *M*1 metastable state accessed optically here may be related.

The profound decoupling of the semiconductor-to-metal transition in mid-IR optical properties and the SPT induced through optical excitation indicates that the PLD of the *M*1 phase is insufficient to fully explain the semiconducting gap. From the perspective of the striking change in electronic properties, the principal role of the PLD is to alter the accessibility of the bands formed by states of d_{xy} symmetry. With the PLD in place, these states are depopulated, and the highest-energy occupied bands have a 1D character and are susceptible to further electronic ordering. The isotropic electronic character of the equilibrium rutile metal (*22*) cannot be realized with the PLD intact. Finally, the large threshold excitation fluence for the SPT relative to that for the observed electronic reorganization demonstrates that the latent heat of the first-order phase transition at ~340 K is dominated by the SPT rather than by the electronic transition.

Our study shows that UED is able to provide deep insights into the nature of other strongly correlated materials through the disparate concurrent responses of active degrees of freedom in the time domain. Further, our results have relevance to the study of the interplay between valence charge and lattice structure in molecular and materials chemistry.

REFERENCES AND NOTES

1. M. Imada, A. Fujimori, Y. Tokura, *Rev. Mod. Phys.* **70**, 1039–1263 (1998).
2. E. Dagotto, *Science* **309**, 257–262 (2005).
3. P. A. Lee, X.-G. Wen, *Rev. Mod. Phys.* **78**, 17–85 (2006).
4. B. J. Siwick, J. R. Dwyer, R. E. Jordan, R. J. D. Miller, *Science* **302**, 1382–1385 (2003).
5. C.-Y. Ruan, Y. Murooka, R. K. Raman, R. A. Murdick, *Nano Lett.* **7**, 1290–1296 (2007).
6. G. Sciaini, R. J. D. Miller, *Rep. Prog. Phys.* **74**, 096101 (2011).
7. M. Gao *et al.*, *Nature* **496**, 343–346 (2013).
8. L. Whittaker, C. J. Patridge, S. Banerjee, *J. Phys. Chem. Lett.* **2**, 745–758 (2011).
9. C. Berglund, H. Guggenheim, *Phys. Rev.* **185**, 1022–1033 (1969).
10. J. Goodenough, *J. Solid State Chem.* **3**, 490–500 (1971).
11. A. Zylbersztejn, N. Mott, *Phys. Rev. B* **11**, 4383–4395 (1975).
12. R. M. Wentzcovitch, W. W. Schulz, P. B. Allen, *Phys. Rev. Lett.* **72**, 3389–3392 (1994).
13. V. Eyert, *Ann. Phys.* **11**, 650–704 (2002).
14. S. Biermann, A. Poteryaev, A. I. Lichtenstein, A. Georges, *Phys. Rev. Lett.* **94**, 026404 (2005).
15. C. Weber *et al.*, *Phys. Rev. Lett.* **108**, 256402 (2012).
16. T. van Oudheusden *et al.*, *J. Appl. Phys.* **102**, 093501 (2007).
17. R. P. Chatelain, V. R. Morrison, C. Godbout, B. J. Siwick, *Appl. Phys. Lett.* **101**, 081901 (2012).
18. M. Gao *et al.*, *Opt. Express* **20**, 12048–12058 (2012).
19. A. Cavalleri, T. Dekorsy, H. Chong, J. Kieffer, R. Schoenlein, *Phys. Rev. B* **70**, 161102 (2004).
20. S. Wall *et al.*, *Phys. Rev. B* **87**, 115126 (2013).
21. T. C. Koethe *et al.*, *Phys. Rev. Lett.* **97**, 116402 (2006).
22. M. W. Haverkort *et al.*, *Phys. Rev. Lett.* **95**, 196404 (2005).
23. A. Hendaoui, N. Émond, S. Dorval, M. Chaker, E. Haddad, *Curr. Appl. Phys.* **13**, 875–879 (2013).
24. See supplementary materials on *Science* Online.
25. A. Cavalleri *et al.*, *Phys. Rev. Lett.* **87**, 237401 (2001).
26. P. Baum, D.-S. Yang, A. H. Zewail, *Science* **318**, 788–792 (2007).
27. A. Pashkin *et al.*, *Phys. Rev. B* **83**, 195120 (2011).
28. T. L. Cocker *et al.*, *Phys. Rev. B* **85**, 155120 (2012).
29. J. M. Zuo, *Rep. Prog. Phys.* **67**, 2053–2103 (2004).
30. J.-C. Zheng, Y. Zhu, L. Wu, J. W. Davenport, *J. Appl. Crystallogr.* **38**, 648–656 (2005).
31. A. M. M. Abeykoon *et al.*, *Z. Kristallogr.* **227**, 248–256 (2012).
32. A. S. Belozerov, M. A. Korotin, V. I. Anisimov, A. I. Poteryaev, *Phys. Rev. B* **85**, 045109 (2012).
33. R. Sakuma, T. Miyake, F. Aryasetiawan, *J. Phys. Condens. Matter* **21**, 064226 (2009).
34. Y. Yao *et al.*, *Mod. Phys. Lett. B* **27**, 1330015 (2013).
35. M. M. Qazilbash *et al.*, *Phys. Rev. B* **83**, 165108 (2011).
36. M. M. Qazilbash *et al.*, *Science* **318**, 1750–1753 (2007).
37. J. Nag, R. F. Haglund, E. A. Payzant, K. L. More, *J. Appl. Phys.* **112**, 103532 (2012).

ACKNOWLEDGMENTS

Supported by Natural Sciences and Engineering Research Council of Canada (NSERC), the Canada Foundation for Innovation, the Canada Research Chairs program, NSERC PGS-D and CGS-D fellowships (R.P.C. and V.M.), and Fonds de Récherche du Québec–Nature et Technologies. We thank C. Weber for insightful discussion regarding the contemporary theoretical treatment of the electronic structure of VO_2.

SUPPLEMENTARY MATERIALS

www.sciencemag.org/content/346/6208/445/suppl/DC1
Materials and Methods
Figs. S1 to S4
References (*38*, *39*)

24 March 2014; accepted 19 September 2014
10.1126/science.1253779

VALLEYTRONICS

Detecting topological currents in graphene superlattices

R. V. Gorbachev,[1,2]* J. C. W. Song,[3,4]* G. L. Yu,[1] A. V. Kretinin,[2] F. Withers,[2] Y. Cao,[1] A. Mishchenko,[1] I. V. Grigorieva,[2] K. S. Novoselov,[2] L. S. Levitov,[3]* A. K. Geim[1,2]†

Topological materials may exhibit Hall-like currents flowing transversely to the applied electric field even in the absence of a magnetic field. In graphene superlattices, which have broken inversion symmetry, topological currents originating from graphene's two valleys are predicted to flow in opposite directions and combine to produce long-range charge neutral flow. We observed this effect as a nonlocal voltage at zero magnetic field in a narrow energy range near Dirac points at distances as large as several micrometers away from the nominal current path. Locally, topological currents are comparable in strength with the applied current, indicating large valley-Hall angles. The long-range character of topological currents and their transistor-like control by means of gate voltage can be exploited for information processing based on valley degrees of freedom.

Berry curvature is a physical field intrinsic to some crystal lattices, which can dramatically affect the transport properties of materials (*1*–*6*). Topological effects, although known for some time (*7*), have gained attention recently in connection with the discovery of topological insulators (*8*–*11*). In these materials, topological bands lead to new phenomena such as topologically protected edge-state transport in zero magnetic field (*12*–*14*). No less striking,

Downloaded from www.sciencemag.org on February 13, 2015

however, is the expected impact of Berry curvature on bulk transport, leading to topological currents flowing perpendicular to the applied electric field E (5, 6). The nondissipative nature of these currents, ensured by their transverse character, resembles that of Hall currents. However, topological currents can arise in the absence of magnetic field B and even without breaking time-reversal symmetry (TRS). In contrast to cyclotron orbits in a magnetic field drifting perpendicular to E, topological currents originate from perfectly straight trajectories that skew left or right relative to E (Fig. 1A). In materials whose electronic structure has more than one valley (4, 15, 16), topological currents in different valleys have opposite signs and, if intervalley scattering is weak, can add up to produce long-range topological charge-neutral currents.

Graphene placed on top of hexagonal boron nitride (G/hBN) (Fig. 1) affords an exceptional venue for inducing and manipulating topological bulk currents at $B = 0$ for the following reasons. First, graphene's band structure possesses a nonzero Berry's phase (17), which is a prerequisite for the existence of Berry curvature. Second, if crystallographic axes of graphene and hBN are aligned, global A/B sublattice asymmetry is introduced (18-20). This gives rise to broken inversion symmetry and a finite Berry curvature. Third, the high electronic quality of graphene protects topological currents against intervalley scattering, allowing them to propagate away from the applied current path. The valley-Hall effect (VHE) creates an electrical response in remote regions, which can be exploited to detect the presence of topological currents experimentally. The nonlocal response is expected whenever the Fermi level in graphene is tuned into one of the Berry curvature hot spots (Fig. 1B). This approach, besides offering a direct probe of topological currents, provides a precision tool for mapping out the Berry curvature in G/hBN Bloch bands. So far, it has proven challenging to probe bulk topological currents without applying B. In particular, this was the case for the anomalous Hall effect in magnetic metals, which was previously perhaps the cleanest system available by which to study topological bands (6).

Experimentally, we studied G/hBN superlattices (in which the graphene and hBN lattices were aligned) fabricated following the procedures described in (21). Fifteen superlattice devices similar to the one shown in the inset of Fig. 1B were investigated. The charge carrier mobilities μ varied from 40,000 to 80,000 $cm^2\ V^{-1}\ s^{-1}$, and the longitudinal and Hall resistivities (ρ_{xx} and ρ_{xy}, respectively) exhibited essentially the same behavior as reported previously (18, 19, 21, 22). Namely, pronounced peaks in ρ_{xx} were observed at the main neutrality point (NP) and at carrier density $n \approx \pm 3 \times 10^{12}\ cm^{-2}$ (Fig. 1B and fig. S1). The peaks in ρ_{xx} were accompanied by a sign reversal of ρ_{xy} indicating the emergence of new NPs in the valence and conduction bands of graphene (18–22). Both encapsulated and nonencapsulated structures were investigated, with the former having an additional hBN crystal placed on top of a G/hBN superlattice to protect it from the environment (20, 21). Some of the latter showed activation behavior at the main NP (fig. S2), yielding a bandgap 2Δ of 350 ± 40 K (20), which is in agreement with earlier transport (18, 19) and spectroscopy (23) measurements. Our encapsulated devices, despite higher electronic quality, exhibited no activation behavior at the main NP, with the ρ_{xx} value saturating at <10 kilohm for temperatures T below 50 K (19, 21). Although this behavior remains to be understood, it is likely that devices that do not show activation behavior in transport properties still have a bandgap (20). In this regard, observing the activation behavior usually relies on midgap impurity states that pin the Fermi level inside the gap (20). However, few midgap states are expected in high-quality G/hBN devices. Alternatively, spatial charge inhomogeneity can "short-circuit" the activation behavior by allowing current to circumnavigate the insulating regions. This would also obscure the activation behavior, leading to metallic-like transport in ρ_{xx}. However, charge inhomogeneity is expected to have relatively little effect on the VHE; being a non–sign-changing function of density (Fig. 1B, inset), it should not average out. Therefore, the activation behavior is not essential for observing topological currents (20). Indeed, both encapsulated and nonencapsulated graphene were found to exhibit very similar nonlocal response.

The central result of our study is shown in Fig. 1B. The nonlocal resistance R_{NL} was determined by applying current between, contacts 4 and 8 and measuring voltage between contacts 3 and 9 (Fig. 1B, micrograph). R_{NL} exhibits large sharp peaks at the main and hole-side NPs (unless stated otherwise, all the presented data refer to zero B). A striking feature of the observed

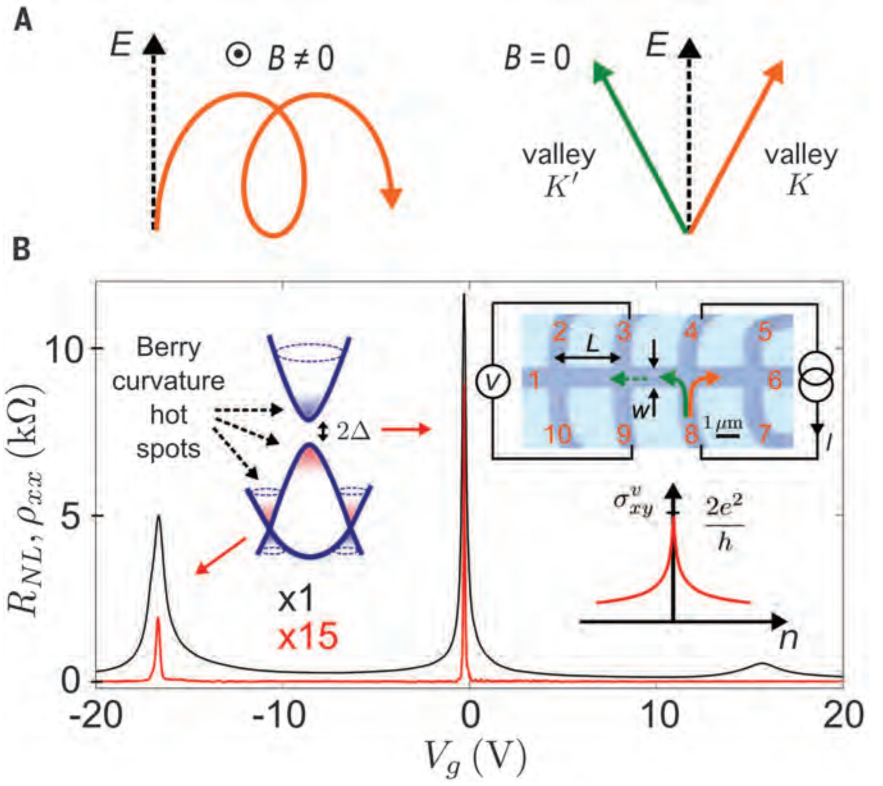

Fig. 1. Detection of long-range valley transport due to topological currents. (**A**) Nontopological and topological Hall currents. (Left) Drifting cyclotron orbits give rise to Hall currents of the same sign for valleys K and K'. (Right) Skewed motion induced by Berry curvature. Trajectories are straight lines directed at nonzero angles to the longitudinal field, having opposite signs for valleys K and K'. The net transverse current, which is charge-neutral, creates a nonlocal charge response via a reverse VHE. (**B**) Nonlocal resistance in graphene superlattices (red curve) and longitudinal resistance (black curve) measured in G/hBN superlattices [graphene aligned on hBN (18–23)]. The back gate voltage V_g was applied through a ≈130-nm-thick dielectric (SiO_2 plus hBN); T = 20 K. (Top right inset) Optical micrograph of our typical G/hBN device and the nonlocal measurement geometry; $L \approx 3.5\ \mu m$, $w \approx 1\ \mu m$. Shown schematically are valley K and K' currents and the long-range response mechanism. (Left inset) Schematic band structure of graphene superlattices, with Berry curvature hot spots arising near the gap opening and avoided band crossing regions (20, 25). (Bottom right inset) Valley Hall conductivity modeled for gapped Dirac fermions as a function of carrier density.

---

[1]Centre for Mesoscience and Nanotechnology, University of Manchester, Manchester M13 9PL, UK. [2]School of Physics and Astronomy, University of Manchester, Oxford Road, Manchester M13 9PL, UK. [3]Department of Physics, Massachusetts Institute of Technology, Cambridge, MA 02139, USA. [4]School of Engineering and Applied Sciences, Harvard University, Cambridge, MA 02138, USA.
*These authors contributed equally to this work. **†Corresponding author. E-mail: levitov@mit.edu (L.S.L.); geim@manchester.ac.uk (A.K.G.)**

nonlocality is its narrow range in n (Figs. 1B and 2A). Unlike ρ_{xx}, which follows the $1/n$ dependence typical for graphene and remains sizeable (>100 ohm) over the entire range of accessible n (Figs. 1 and 2 and fig. S1), R_{NL} decays rapidly with n and completely disappears under noise for densities $>10^{11}$ cm^{-2} away from the NPs. The dependence can be approximately described by $R_{NL} \propto 1/|n|^{\alpha}$, with $\alpha \approx 2.5$ to 3 (Fig. 2B). A nonlocal voltage can also appear because of stray charge currents, described by the van der Pauw relation $R_{NL} \sim \rho_{xx}\exp(-\pi L/w)$, where L is the distance between the current path and voltage probes and w is the device width (Fig. 1B, micrograph) (*24*). For typical aspect ratios $L/w \approx 4$, the formula yields ≈0.01 ohm. The magnitude of this contribution and its n dependence, which follows $\rho_{xx}(n)$, are clearly incompatible with the observed nonlocal response.

We have also investigated how R_{NL} depends on L and found an exponential dependence $\exp(-L/\xi)$ with $\xi \approx 1.0$ μm (Fig. 2C). This ξ value is close to w and much larger than the elastic mean free path of ≈0.1 μm estimated from μ for the range of n where R_{NL} appears. Furthermore, R_{NL} exponentially decreases with increasing temperature T so that no nonlocal signal is detected above 150 K, whereas ρ_{xx} remains large at this T at the main NP (figs. S2 and S3). Nonencapsulated devices exhibited practically the same behavior of R_{NL} as a function of n and T (fig. S4), but the absolute value of R_{NL} was somewhat smaller than that in encapsulated devices (*20*). In addition, we investigated the effect of charge inhomogeneity δn on R_{NL}, which was controlled by sweeping to progressively larger gate voltages V_g beyond the hole-side NP (*20*). When δn was increased by a factor of ≈2, R_{NL} could sometimes change by more than an order of magnitude (*20*). The inhomogeneity enhanced R_{NL} at the main NP and suppressed it at the hole-side NP (fig. S5). The difference is attributed to a narrow energy width of the secondary Dirac spectrum (*20*).

To confirm the key role played by Berry curvature, we verified that the nonlocal response was absent in G/hBN systems without alignment and, accordingly, with no detectable superlattice effects (*18*–*22*). This is illustrated in Fig. 2A, which shows R_{NL} for aligned and nonaligned devices with the same μ and in the same geometry. In the nonaligned devices (>20 measured), no nonlocal signal could be observed even at our maximum resolution of ~0.1 ohm (Fig. 2A, blue curve). Therefore, the observed R_{NL} cannot be explained by charge-neutral flow of spin and/or energy, which are indifferent to crystal alignment. The latter flows also require broken TRS and completely disappear in zero B, as reported previously (*24*–*26*). In our superlattice devices, a contribution of spin/energy flows becomes appreciable only for $B > 0.1$ T (fig. S6), leading to rapid broadening of the R_{NL} peaks, which is in agreement with (*24*).

We have also considered the possibility that the observed nonlocality at $B = 0$ may originate from an edge transport mechanism. For example, topological materials can support gapless edge modes that coexist with the gapped bulk. Such modes could in principle mediate nonlocal charge transport. However, our experiments provide no evidence for metallic conductivity along the device edges. First, the measured nonlocal response was similar for all our devices, independent of whether they exhibited metallic or insulating behavior in ρ_{xx}. Second, atomic force microscopy studies show that the moiré pattern associated with the alignment extends all the way to the device edges, and there are no distinct edge regions (*19*). Third, extrapolating the dependence in Fig. 2C to small L, we found that the edge transport scenario would require metallic conductivity along edges of $\approx 2e^2/h$ over distances of $L > 1$ μm. This would imply perfect edge-state transport, which is unlikely at such length scales in the presence of strong intervalley scattering expected at microscopically rough edges.

Proceeding with the analysis, the aligned superlattices are comprised of hexagonal unit cells, each representing a commensurate graphene/hBN region of ~10 nm in size, which is surrounded by a strained boundary (*19*). All unit cells are characterized by A/B sublattice asymmetry of the same sign, giving a preferred chirality over the entire structure (*19*, *20*, *25*). For our typical $n < 10^{11}$ cm^{-2}, Fermi wavelengths are larger than 100 nm, which exceeds the superlattice periodicity by a factor of ~10. This large wavelength/period ratio renders contributions from spatially varying couplings insubstantial.

We will show below that the observed nonlocality features are consistent with bulk topological currents expected for a gapped Dirac spectrum. The mechanism by which Berry curvature generates topological currents can be elucidated by the semiclassical equations of motion (*5*)

$$\hbar\dot{k} = eE + ev(k)\times B,$$

$$v(k) = \frac{1}{\hbar}\frac{\partial\epsilon(k)}{\partial k} + \dot{k}\times\Omega(k) \qquad (1)$$

where Ω is the Berry curvature density and $v(k)$ is the group velocity of Bloch electrons. The Lorentz force term $ev \times B$ describes the conventional Hall effect. Berry curvature gives rise to an "anomalous velocity," $\dot{k} \times \Omega(k)$, which is of the same structure as the Lorentz term but in momentum space and leads to transverse currents (Fig. 1A). Such currents may appear in zero B [without breaking TRS that requires $\Omega(k) = -\Omega(-k)$] as long as inversion symmetry is broken, $\Omega(k) \neq \Omega(-k)$, as is the case of our aligned devices with globally broken A/B sublattice symmetry (*19*). For $B = 0$, transverse currents arise solely from $\Omega(k)$, yielding Hall-like conductivity σ_{xy} given by the sum of Berry fluxes for all occupied states in the Fermi sea (*3*)

$$\sigma_{xy} = 2\frac{e^2}{h}\int\frac{d^2k}{2\pi}\Omega(k)f(k) \qquad (2)$$

with $f(k)$ being the Fermi function and the factor of 2 accounting for spin degeneracy. Because Berry

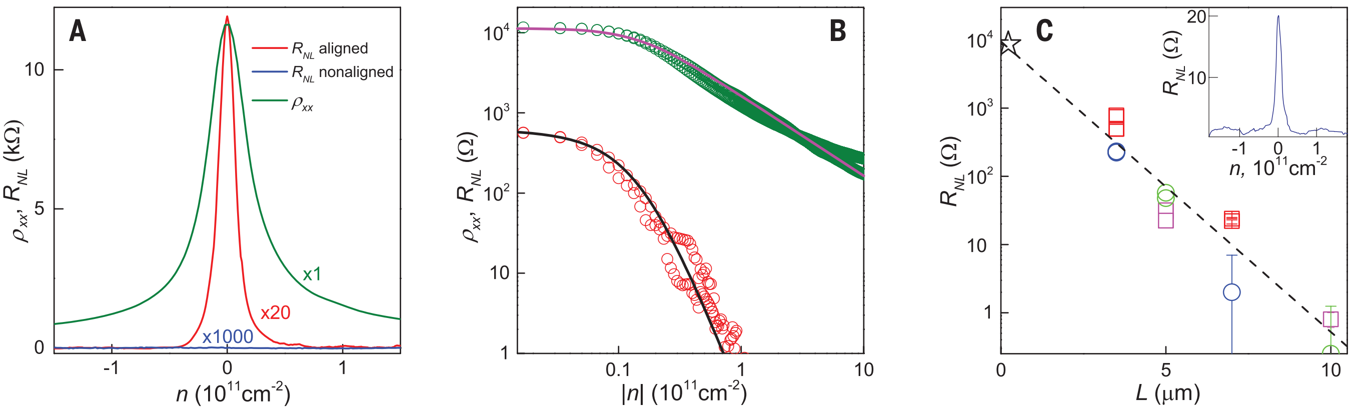

Fig. 2. Density and distance dependences for nonlocal valley currents. (**A**) Behavior of ρ_{xx} and R_{NL} near the main NP in superlattice devices (green and red, respectively). The blue curve is for a nonaligned, reference device (≈10° misalignment between graphene and hBN crystal axes). $L \approx 3.5$ μm; $w \approx 1$ μm; $T = 20$ K. (**B**) The same data as (A) on a logarithmic scale. Away from the NP, ρ_{xx} exhibits the conventional $1/n$ dependence (green symbols) and can be described by $\rho_{xx}(n) \propto 1/(n^2 + \delta n^2)^{1/2}$, where $\delta n \approx 1.5 \times 10^{10}$ cm^{-2} accounts for charge inhomogeneity (light purple line). Measured R_{NL} (red symbols) and the Berry curvature model (black curve, Eq. 3). Model uses the above δn and bandgap $2\Delta = 360$ K found from local measurements (*18*–*20*). (**C**) Nonlocal signal decays exponentially with increasing L. Color refers to similar devices with the same L or the same device with two different L; $w \approx 1$ μm, 20 K; 10 devices in total. The black star is the anomalous contribution to ρ_{xx} observed in the bend geometry, which is consistent with strong topological currents induced locally (*20*). (Inset) R_{NL} remains sizeable at $L \approx 7$ μm.

curvature is odd in energy (*20*), σ_{xy} has the same sign for both electrons and holes. This contrasts with the conventional Hall conductivity that is sign-changing under carrier-type reversal. As a result, σ_{xy} given by Eq. 2 is less susceptible to smearing by inhomogeneity. This mechanism yields a nonzero R_{NL} whenever the Fermi level is tuned through Berry curvature hot spots. Their extent in energy is given by half the bandgap $\Delta \approx 180$ K, which translates into $n \approx 2 \times 10^{10}$ cm^{-2} and agrees well with the ultranarrow width of our R_{NL} peaks.

Because of TRS, the electric field generates topological currents (Eq. 1) with opposite transverse components in graphene's two valleys, K and K' (Fig. 1A), to create the charge-neutral VHE, $J_v = J_K - J_{K'} = \sigma^v_{xy}E$, where $\sigma^v_{xy} = 2\sigma_{xy}$. As illustrated in the inset to Fig. 1B, topological currents can result in a VHE conductivity of $\approx 2e^2/h$. In the absence of intervalley scattering, the charge-neutral currents can persist over extended distances and mediate nonlocal electrical signals (*24*–*28*). The resulting nonlocal resistance R_{NL} can be understood as originating from the VHE and a reverse VHE (*20*), by analogy with nonlocal transport mediated by charge-neutral spin or energy flow (*24*–*28*). Yet unlike the latter, the VHE-induced nonlocality appears without TRS breaking—that is, at zero B. This behavior, as well as the narrow range of n over which R_{NL} is observed, is a telltale sign of bulk topological currents. The analysis outlined above yields the model expression (*20*)

$$R_{\mathrm{NL}} = (w/2\xi)(\sigma^v_{xy})^2\rho^3_{xx}\exp(-L/\xi) \qquad (3)$$

The peak in $R_{\mathrm{NL}}(n)$ can be described by Eq. 3 with no fitting parameters (Fig. 2B).

The measured spatial decay with $\xi \approx 1.0$ μm is consistent with intervalley scattering occurring at graphene edges and/or at atomic-scale defects (*20*). The large values of R_{NL} at L of several micrometers also imply extremely strong topological currents locally, within the path of the applied current. By extrapolating the observed L dependence to $L < 1$ μm, Fig. 2C yields R_{NL} ~10 kilohm. According to Eq. 3, this translates into $\sigma^v_{xy} \approx 2e^2/h$ and order-one Hall angles, which is in agreement with the VHE expected for weak intervalley scattering. Furthermore, similar to classical magnetotransport, changes in the direction of current flow can lead to additional resistivity. For $\sigma_{xy}\rho_{xx} \sim 1$, the classical magnetoresistance reaches a value of ~ρ_{xx} when carriers of opposite sign are involved. A valley analog of this extra resistance may explain anomalous contributions of ~10 kilohm in ρ_{xx}, which are observed at short distances $L \approx w$ by using the bend geometry (fig. S7). Parenthetically, the intrinsic VHE mechanism discussed above, which provides excellent agreement with our experimental results, may coexist with extrinsic VHE mechanisms such as skew scattering and side jumps (*6*). Although their role in graphene superlattices remains to be examined, such mechanisms also originate from Berry curvature and arise under the same symmetry conditions as the intrinsic contribution.

Last, sharp changes in R_{NL} with V_{g} (130-nm-thick dielectric) (Figs. 1 and 2) amount to a transistor-like response with a slope of ≈100 mV/dec—that is, the detected voltage changes by a factor of 10 by varying V_{g} by ≈100 mV. Although the peaks in R_{NL} broaden with increasing T and disappear above 100 K (because of the relatively small Δ), one can envision electronic devices based on the valley degrees of freedom (*29*), which would become practical if larger bandgap values are achieved. To explore this further, we fabricated a superlattice device with a short top gate (15-nm dielectric) placed between the current and voltage contacts used for nonlocal measurements (fig. S8). Valley currents in this case could be switched on and off, similar to the case of a field effect transistor, by a gate voltage of ≈10 mV at 20 K (*20*). It is feasible to further reduce the thickness of the top gate hBN dielectric down to 2 nm, which would translate into a gate response down to <2 mV/dec at this T. Although further analysis is necessary, these results may indicate that subthreshold slopes better than those achievable for conventional charge-based processing devices (*30*) are possible.

REFERENCES AND NOTES

1. W. Kohn, J. M. Luttinger, *Phys. Rev.* **108**, 590–611 (1957).
2. G. Sundaram, Q. Niu, *Phys. Rev. B* **59**, 14915–14925 (1999).
3. F. D. M. Haldane, *Phys. Rev. Lett.* **93**, 206602 (2004).
4. D. Xiao, W. Yao, Q. Niu, *Phys. Rev. Lett.* **99**, 236809 (2007).
5. D. Xiao, M.-C. Meng, Q. Niu, *Rev. Mod. Phys.* **82**, 1959–2007 (2010).
6. N. Nagaosa, J. Sinova, S. Onoda, A. H. MacDonald, N. P. Ong, *Rev. Mod. Phys.* **82**, 1539–1592 (2010).
7. J. Zak, *Phys. Rev. Lett.* **62**, 2747–2750 (1989).
8. C. L. Kane, E. J. Mele, *Phys. Rev. Lett.* **95**, 226801 (2005).
9. B. A. Bernevig, T. L. Hughes, S. C. Zhang, *Science* **314**, 1757–1761 (2006).
10. L. Fu, C. L. Kane, E. J. Mele, *Phys. Rev. Lett.* **98**, 106803 (2007).
11. R. Roy, *Phys. Rev. B* **79**, 195322 (2007).
12. M. König *et al.*, *Science* **318**, 766–770 (2007).
13. C. Z. Chang *et al.*, *Science* **340**, 167–170 (2013).
14. D. Hsieh *et al.*, *Science* **323**, 919–922 (2009).
15. D. Xiao, G. B. Liu, W. Feng, X. Xu, W. Yao, *Phys. Rev. Lett.* **108**, 196802 (2012).
16. K. F. Mak, K. L. McGill, J. Park, P. L. McEuen, *Science* **344**, 1489–1492 (2014).
17. T. Ando, T. Nakanishi, R. Saito, *J. Phys. Soc. Jpn.* **67**, 2857–2862 (1998).
18. B. Hunt *et al.*, *Science* **340**, 1427–1430 (2013).
19. C. R. Woods *et al.*, *Nat. Phys.* **10**, 451–456 (2014).
20. Materials and methods are available as supplementary materials on *Science* Online.
21. L. A. Ponomarenko *et al.*, *Nature* **497**, 594–597 (2013).
22. C. R. Dean *et al.*, *Nature* **497**, 598–602 (2013).
23. Z. G. Chen *et al.*, *Nat. Commun.* **5**, 4461 (2014).
24. D. A. Abanin *et al.*, *Science* **332**, 328–330 (2011).
25. J. C. W. Song, P. Samutpraphoot, L. S. Levitov, Topological bands in G/hBN heterostructures. http://arxiv.org/abs/1404.4019 (2014).
26. J. Renard, M. Studer, J. A. Folk, *Phys. Rev. Lett.* **112**, 116601 (2014).
27. M. Titov *et al.*, *Phys. Rev. Lett.* **111**, 166601 (2013).
28. D. A. Abanin, A. V. Shytov, L. S. Levitov, B. I. Halperin, *Phys. Rev. B* **79**, 035304 (2009).
29. A. Rycerz, J. Tworzydlo, C. W. J. Beenakker, *Nat. Phys.* **3**, 172–175 (2007).
30. S. M. Sze, K. K. Ng, *Physics of Semiconductor Devices* (Wiley, New York, 2007), chap. 6.

ACKNOWLEDGMENTS

This work was supported by the European Research Council, the Royal Society, the Office of Naval Research, the Air Force Office of Scientific Research, the Engineering and Physical Sciences Research Council (UK), and the National Science Foundation.

SUPPLEMENTARY MATERIALS

www.sciencemag.org/content/346/6208/448/suppl/DC1
Materials and Methods
Supplementary Text
Figs. S1 to S8
References (*31*–*37*)

17 April 2014; accepted 29 August 2014
Published online 11 September 2014;
10.1126/science.1254966

ASYMMETRIC CATALYSIS

Room-temperature enantioselective C–H iodination via kinetic resolution

Ling Chu, Kai-Jiong Xiao, Jin-Quan Yu*

Asymmetric carbon-hydrogen (C–H) activation reactions often rely on desymmetrization of prochiral C–H bonds on the same achiral molecule, using a chiral catalyst. Here, we report a kinetic resolution via palladium-catalyzed enantioselective C–H iodination in which one of the enantiomers of a racemic benzylic amine substrates undergoes faster aryl C–H insertion with the chiral catalysts than the other. The resulting enantioenriched C–H functionalization products would not be accessible through desymmetrization of prochiral C–H bonds. The exceedingly high relative rate ratio ($k_{\mathrm{fast}}/k_{\mathrm{slow}}$ up to 244), coupled with the subsequent iodination of the remaining enantiomerically enriched starting material using a chiral ligand with the opposite configuration, enables conversion of both substrate enantiomers into enantiomerically pure iodinated products.

A wide range of C–H activation reactions have emerged as promising tools for organic synthesis over the past two decades. However, the development of enantioselective C–H activation reactions has met with limited success in terms of efficiency and scope (*1*). Enantioselective carbene insertions into prochiral methylene C–H bonds adjacent to heteroatoms have been achieved in synthetically useful enantioselectivity (*2*). Asymmetric nitrene insertion has also been demonstrated in both diastereoselective and enantioselective

Detecting topological currents in graphene superlattices
R. V. Gorbachev *et al.*
Science **346**, 448 (2014);
DOI: 10.1126/science.1254966

This copy is for your personal, non-commercial use only.

If you wish to distribute this article to others, you can order high-quality copies for your colleagues, clients, or customers by clicking here.

Permission to republish or repurpose articles or portions of articles can be obtained by following the guidelines here.

The following resources related to this article are available online at www.sciencemag.org (this information is current as of February 13, 2015):

Updated information and services, including high-resolution figures, can be found in the online version of this article at:
http://www.sciencemag.org/content/346/6208/448.full.html

Supporting Online Material can be found at:
http://www.sciencemag.org/content/suppl/2014/09/10/science.1254966.DC1.html

A list of selected additional articles on the Science Web sites **related to this article** can be found at:
http://www.sciencemag.org/content/346/6208/448.full.html#related

This article **cites 34 articles**, 8 of which can be accessed free:
http://www.sciencemag.org/content/346/6208/448.full.html#ref-list-1

This article has been **cited by** 1 articles hosted by HighWire Press; see:
http://www.sciencemag.org/content/346/6208/448.full.html#related-urls

This article appears in the following **subject collections:**
Physics
http://www.sciencemag.org/cgi/collection/physics

Downloaded from www.sciencemag.org on February 13, 2015

Science (print ISSN 0036-8075; online ISSN 1095-9203) is published weekly, except the last week in December, by the American Association for the Advancement of Science, 1200 New York Avenue NW, Washington, DC 20005. Copyright 2014 by the American Association for the Advancement of Science; all rights reserved. The title *Science* is a registered trademark of AAAS.